

Aeroelastic-aerodynamic analysis and bio-inspired flow sensor design for boundary layer velocity profiles of wind turbine blades with active external flaps

Xiao Sun¹, Junliang Tao², Jiale Li³, Qingli Dai^{*1} and Xiong Yu³

¹Department of Civil and Environmental Engineering, Michigan Technological University, 1400 Townsend Drive, Houghton, MI 49931, USA

²Department of Civil Engineering, The University of Akron, 244 Sumner St., Akron, OH, 44321-3905, USA

³Department of Civil Engineering, Case Western Reserve University, 2104 Adelbert Road, Bingham Building-Room 206, Cleveland, OH 44106, USA

(Received May 5, 2016, Revised July 11, 2017, Accepted July 17, 2017)

Abstract. The characteristics of boundary layers have significant effects on the aerodynamic forces and vibration of the wind turbine blade. The incorporation of active trailing edge flaps (ATEF) into wind turbine blades has been proven as an effective control approach for alleviation of load and vibration. This paper is aimed at investigating the effects of external trailing edge flaps on the flow pattern and velocity distribution within a boundary layer of a NREL 5MW reference wind turbine, as well as designing a new type of velocity sensors for future validation measurements. An aeroelastic-aerodynamic simulation with FAST-AeroDyn code was conducted on the entire wind turbine structure and the modifications were made on turbine blade sections with ATEF. The results of aeroelastic-aerodynamic simulations were combined with the results of two-dimensional computational fluid dynamic simulations. From these, the velocity profile of the boundary layer as well as the thickness variation with time under the influence of a simplified load case was calculated for four different blade-flap combinations (without flap, with -5° , 0° , and $+5^\circ$ flap). In conjunction with the computational modeling of the characteristics of boundary layers, a bio-inspired hair flow sensor was designed for sensing the boundary flow field surrounding the turbine blades, which ultimately aims to provide real time data to design the control scheme of the flap structure. The sensor element design and performance were analyzed using both theoretical model and finite element method. A prototype sensor element with desired bio-mimicry responses was fabricated and validated, which will be further refined for integration with the turbine blade structures.

Keywords: active external trailing edge flap; wind turbine; boundary layer; hair flow sensor; aerodynamic; aeroelastic

1. Introduction

The size of wind turbine has increased rapidly in recent decades due to the progress in composite materials, advanced fabrication methods, and design and analytical tools. As the result, the power generation from wind turbine has been effectively improved. However, the growing size of the rotor inevitably causes higher load and vibrations of the wind turbine components. Therefore, load and vibration reductions are essential to extending the turbine service life and preventing related catastrophic failures.

Taking the advantages of smart material based actuators, active trailing edge flap (ATEF) along with other smart rotor control techniques has been widely studied for wind turbine load alleviations, as stated in review papers (Barlas and Van Kuik 2010, van Wingerden *et al.* 2008). Various forms of ATEFs have been designed (Løgstrup Andersen *et al.* 2015, Daynes and Weaver 2012, Basualdo 2005).

Aeroelastic models have been established such that the loads and deformation of blade with ATEFs can be

accurately investigated (Buhl *et al.* 2005a, Buhl *et al.* 2005b, Basualdo 2005, Barlas and Van Kuik 2009, Gillebaart *et al.* 2014). The fatigue load reduction, aerodynamic efficiency, response bandwidth and complexity of ATEF control were compared with other control methods such as micro-electro-mechanical tab control, active blade twist control and camber control (Marrant and Van Holten 2006). Control schemes of ATEFs have been proposed and evaluated to effectively reduce the loads and vibration (Wilson *et al.* 2010, Henriksen *et al.* 2013, Ng *et al.* 2014, Lackner and van Kuik 2010). Both numerical simulations (Wilson *et al.* 2009) and field tests (Berg *et al.* 2013, Castaignet *et al.* 2014) have demonstrated the load alleviation potential of ATEFs for wind turbine applications.

In order to study the effects of the ATEFs on the flow pattern around the wind turbine blades, the flow pattern and velocity characteristics of boundary layer are of particular interest, since the flow within the boundary layer plays an important role in aerodynamic problems, such as the skin friction drag and flow separation. Laminar and turbulent are the two types of boundary layers depending on the value of the Reynolds number. For a modern megawatt wind turbine, the Reynolds number can easily reach $8E6$ to $10E6$ (Timmer and Schaffarczyk 2004). For a typical airfoil, it

*Corresponding author, Associate Professor
E-mail: qingdai@mtu.edu

tends to have a smooth laminar boundary flow at the leading edge. After flowing some distance from the leading edge, the laminar flow gradually transitions to a turbulent boundary layer flow. Since the laminar/turbulence properties of boundary layer have a significant impact on skin friction, flow separation and aerodynamic characteristics, the boundary layer has been widely investigated (Abbott and Von Doenhoff 1959, Bermúdez *et al.* 2002, Brendel and Mueller 1988, Devinant *et al.* 2002, Garcia-Sagrado and Hynes 2012, Gleyzes and Capbern 2003, Michael *et al.* 2011). These studies all involved traditional wind tunnel tests on a particular airfoil. Particularly, the velocity profiles were collected using hot-wire velocity probe and laser doppler velocimetry (LDV), as well as flow visualization techniques. The conventional hot-wire velocity probe has to be placed into the flow to take measurements, therefore it inevitably alters the flow to some extent. In addition, the hot-wire probe must be calibrated before use and is extremely brittle. The LDV is superior to the hot-wire probe since it is non-intrusive. However, LDV systems are more expensive and most of them require optical access and seeding. At the same time, tufts and flow cones are attached to an airfoil surface for visualizing the flow direction and flow separation (Fisher and Meyer Jr. 1988). When the dynamic pressure is sufficient, they are aligned with the local flow stream and reveal the local flow pattern. Tufts are relatively small strings made of nylon or wool. Compared to flow cones, they have some disadvantages including the instability and low visibility at distances. Flow cones are rigid and hollow conical shaped with a string at the apex of the cone. They are more visible than tufts owing to their larger dimensions and reflective character. Due to current issues, there is a need to develop an innovative flow velocity and pattern sensor that is non-intrusive, sensitive, and stable in harsh environments.

Bio-inspired sensing principles are promising to overcome the current limitations. Many fishes, such as salmon, and birds have developed keen sense of flow motion. This helps them orient to unsteady flow and therefore reduces the flow resistance, a phenomena referred to as rheotaxis (Montgomery *et al.* 1997). It has long been conjectured that the lateral line on the fish body, which consists of an array of hairy cells, allows the sensing of flow, since experiments have found that fish will be unable to orient themselves if the lateral line is removed or damaged (Bleckmann 1994). Research has found that the lateral line is composed of two types of sensors: canal neuromasts and peripheral neuromasts. The canal neuromasts stick out into the flow, while the peripheral neuromasts respond to adjacent flow (Coombs and Fay 1989). There were debates over how the lateral line senses the water motion. It was recently found that the lateral line is a turbulence sensor, where it senses flow not due to the steady component, but due to the turbulence component (Chagnaud *et al.* 2008a). By measuring the signals from pairs of neuromasts in the lateral line of goldfishes, researchers found fish estimates the flow speed by sensing the time delay as turbulence passes different neuromasts (Chagnaud *et al.* 2008b).

The use of sensor array to detect turbulent flow has emerged in the last few years (Bruker *et al.* 2005, Glassmaker *et al.* 2014). It is based on detecting the propagation of flow disturbance along individual pillars in the array. From the spatial coding and time domain correlation analysis, the pattern of a turbulent flow can be readily determined. One of the advantages of such sensor arrays is to sense the spatial distribution of turbulence. A few factors need to be considered when designing the spacing between sensors, i.e., the lateral collapse and flow interference. *Lateral collapse* is a phenomenon for filiform structures in an array. If pillars are brought together due to external forces, they tend to remain connected. This can be prevented by separating the pillars with enough spacing (Glassmaker *et al.* 2004). *Flow interference* is another important factor in array design. Brucker *et al.* (2005) showed that flow interference decays to below 5% for distances greater than the length of the sensor. As a result, the spacing should be related to the length of the micro pillar. This spacing should also satisfy the lateral collapse criterion.

In this study we aim to develop hair flow sensors design framework based on the information gathered from a wind-blade interaction simulation and demonstrate the feasibility of the hair flow sensors on characterizing the boundary velocity and direction through testing with a prototype. In authors' recent studies, the computation fluid dynamic (CFD) simulation has been conducted to analyze the aerodynamic force applied on the blade as well as the flow pattern around the NREL 5MW reference wind turbine (RWT) blades, which represents a well-known and widely investigated benchmark, as reported in (Menon *et al.* 2016).

The mechanical design and control scheme of an external active trailing edge flap for NREL 5MW RWT blades has been analyzed, which were described in a separated paper (Sun *et al.* 2017). Besides, the structural response was investigated and compared with the original NREL 5MW RWT to evaluate the load reduction potential.

The input values needed for this work are based on the well documented and validated studies of NREL 5MW RWT (Jonkman *et al.* 2009). For a detailed coverage of the related information, the readers are referred to those published works. In Section 2, the wind-blade aeroelastic-aerodynamic simulation was conducted to investigate the local flow characteristics of NREL 5MW RWT blades with external trailing edge flaps due to the rotational motion. Section 3 combined the aerodynamic results with CFD results to calculate the boundary layer velocity profile and thickness, providing valuable information to the design of the bio-inspired hair flow sensor. Section 4 described the design criteria and process for the prototype bio-inspired hair flow sensor. A holistic simulation-based analysis on sensor performance considering geometry and material properties was conducted. Based on the analysis, the sensor prototype was designed. The relationship between the sensor voltage output and the boundary velocity was determined. In the longer term, this bio-inspired sensor can be scaled and mounted to the blade-flap system in a way similar to tufts and be subjected to field test or wind tunnel test to further validate its performance. The flow conditions

monitored by the sensor will allow to adjust the operation of the flap structure to achieve the best performance. The continued synergies of the simulation, actuation, and sensing will allow the development of strategies for blade vibration reduction. The research reported in this paper is to develop the simulation scheme and sensor design protocol, which will be further integrated into an integrated sensing-control system for developing smart turbine blades.

2. Aeroelastic-aerodynamic simulation of turbine blade-flap system using FAST-AeroDyn

The local flow characteristics caused by the wind-blade interaction and blade rotational motion are needed in order to design the bio-inspired hair flow sensor for future in-situ evaluation of the performance of a NREL 5MW RWT blade integrated with external trailing edge flaps. Although this information can be gathered from wind tunnel tests or field testing data, computation simulations are more effective and economic especially during the design stage to gain some basic information. There is a variety of aeroelastic codes available for the wind turbine research (Bossanyi 1996, Larsen and Hansen 2007, Øye 1999). The U.S. National Renewable Energy Laboratory (NREL) developed a comprehensive aeroelastic simulation tool called FAST, which stands for Fatigue, Aerodynamic, Structures and Turbulence. It is capable of analyzing the dynamic structural behavior and the energy production of two-bladed and three-bladed horizontal-axis wind turbines (HAWTs). AeroDyn is an aerodynamic code designed to interface with FAST and other aeroelastic simulation codes. In this section, computational simulations using FAST-AeroDyn code were conducted to analyze the relative wind velocity, angle of attack and induction factor experienced by the blade section during the real operation stage. Detailed descriptions of FAST and AeroDyn's functionalities are covered by technical reports (Jonkman and Buhl Jr. 2005, Laino and Hansen 2002). The basic theory of FAST and AeroDyn are described in manuals (Moriarty and Hansen 2005, Jonkman, to be published).

2.1 Model description and input parameters

The FAST and AeroDyn codes use Kane's structural dynamic equations and BEM theory based aerodynamic models to simulate the aerodynamic and structural response of a three-bladed HAWT. Fig. 1 shows a non-dimensionalized airfoil section of the NREL 5MW RWT blade with an external flap. In order to effectively enhance the aerodynamic performance and alleviate the blade loads, a comprehensive research project of adaptive trailing edge aerodynamic devices conducted at Denmark Risø National Laboratory (Basualdo 2005, Buhl *et al.* 2007, Castaignet *et al.* 2014, Bergami *et al.* 2013) suggests that these devices should be applied to the outboard section of wind turbine blades. This is due to the fact that the inboard sections of wind turbine blade mainly serve as structural components to ensure the blade can sustain loads without a large deflection. While the outboard sections mainly serve as

aerodynamic components. The main airfoil profiles used for the outboard section of the NREL 5MW RWT is NACA64₃-618. By covering the 30% of the blade, it provides significant influences on the aerodynamic characteristics of the blade. Therefore, it serves as the target section in this study. The generic analysis approach presented in the following context is based on a typical blade section at 59 m radial location, whose chord length is 2 m. Four simulation models were set up for the four different wind turbine blade-flap combinations respectively: the original 5MW NREL wind turbine blade without external flaps (Case 1); the same blade with external flaps oriented at -5° flap angle (Case 2); at 0° flap angle (Case 3); at +5° flap angle (Case 4). Since this study only provides an estimation for the tentative design of the hair cell flow sensor, the dynamic control scheme of the flap was excluded and the flap was treated as stationary for simplicity's sake.

Various inputs were specified based on the wind turbine model analyzed in this study. The platform was assumed to be firmly fixed to the ground with no translational and rotational motions. No mooring or foundation elasticity was considered. In addition, no hydrostatic or hydrodynamic forces were applied on the foundation. A relatively simple inflow condition was defined at hub height by assuming the incoming wind is uniformly distributed at the computational region and has a constant mean wind speed with a small fluctuation. Under this circumstances, the wind turbine structure behaves almost linearly. Otherwise, the spatial variation of wind speed or significant time variation of mean wind speed inevitably invoke the structural non-linearity of operating wind turbine, which is inherently complex to analysis. The wind speed and rotor speed were assumed to be the rated wind speed and the rated rotor speed of 5MW wind turbine, which are 11.4 m/s and 12.1 rpm (Jonkman *et al.* 2009), respectively. In order to maintain constant rotor speed, the DOFs of generator and drivetrain were disabled, leaving total 17 DOFs. Besides, the total simulation time was 300 seconds with a 0.0125 second time increment. The blade pitch control was disabled. This allows us to analyze a relative simple operation scenery to understand the local flow characteristics. It should be noted that wind is stochastic and wind turbine is subjected to active control method such as blade pitch control in real situations. However, the assumptions do not significantly impair our results. Small turbulences of the mean wind speed was considered implicitly through employing industrial standard turbulence model in our CFD study, as detailed in (Menon *et al.* 2016).

The turbulence can be expressed as a fluctuation of Reynolds number. For the NREL 5MW RWT, the normal operating Reynolds number of the targeted blade section is between 6E+6 and 8.5E+6 (Jonkman *et al.* 2009, Ge *et al.* 2015). A high Reynolds number results in a large portion of turbulent boundary layers at the airfoil surface. Therefore, the shear stress transport version of k- ω turbulence model (Menter 1994), which is known to efficiently simulation flows with high adverse pressure gradient and separated flows, along with high Reynolds number near-wall treatment (ANSYS® Academic Research 2014, Bredberg, 2000) was finally adopted. In this way, both the turbulence

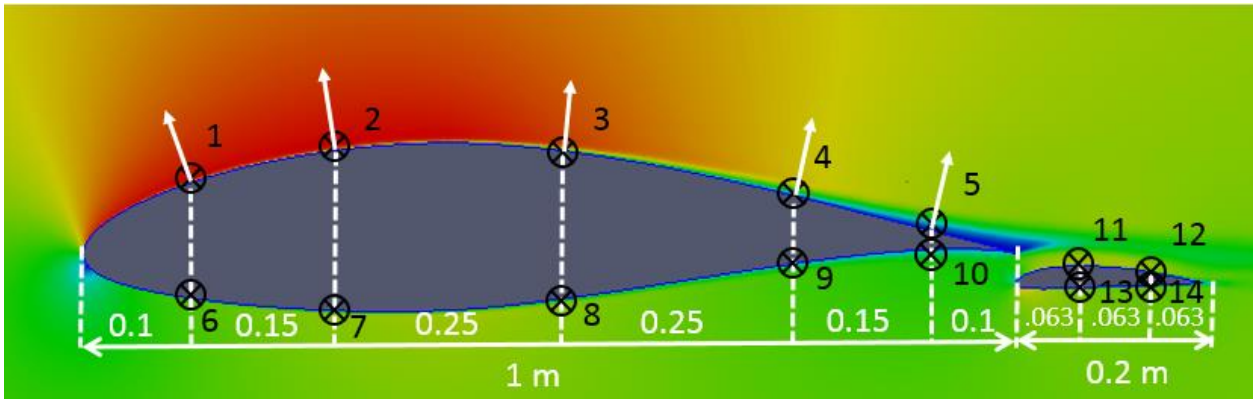


Fig. 1 The sectional blade -external flap layout (non-dimensionalized), the cross marks indicate the proposed flow sensor locations

in the near-wall regions and the flow away from the wall can be better captured.

The active control is actually beneficial for the hair cell sensor application. The blade pitch controller reduces the angle of attack and ensure the blade is operated in the non-stall flow region, thereby preventing the flow from separation. Once the large flow separation occurs, the boundary layer no longer exists and the hair cell sensor is not able to measure the boundary velocity. The situation considered here is actually a more conservative case.

The basic input parameters for FAST and AeroDyn for the 5MW NREL RWT were referred to the documented NREL technical reports (Jonkman *et al.* 2009). This information includes the structural properties, mass properties, aerodynamic characteristics of the tower and blades, etc. Several modifications are necessary to reflect the incorporation of external flaps. For the blade structural properties, the incorporation of external flaps inevitably changes the mass and stiffness distributions (Sun *et al.* 2017). The mass of the external flap, actuators system and supports was assumed to be uniformly distributed across the blade section attached. The stiffness contribution of the external flap to the original blade was neglected for following reasons: (1) the flap stiffness is around 3% of the sectional stiffness of the original blade; (2) the attachment between flap and blade is flexible such that the entire flap only act as an aerodynamic component rather than a major load carrying part. In addition, since the flap actuation range is small, the effects of different flap angles on the stiffness were also assumed to be negligible. Therefore, Case 2-4 share the same blade structural properties. In other words, there were two groups of blade properties: Model I blade was used for simulation in Case 1 and Model II blade was used for Case 2-4.

The next step was to import the aerodynamic coefficients for Cases 1-4. For the original blade in Case 1, the aerodynamic coefficients of each discretized blade element are provided in the test example of FAST code for 5MW NREL wind turbine, originally taken from reference (Kooijman *et al.* 2003). For Case 2-4, three sets of aerodynamic coefficients need to be specified for the NACA 64-618 blade with three different flap angles (-5° , 0° ,

$+5^\circ$). These coefficients have been computed using CFD simulation, which has reported in another published paper (Menon *et al.* 2016). Since the CFD was carried out on the two-dimensional airfoil, aerodynamic coefficients need to be corrected to take three-dimensional stall delay and dynamic stall effects into consideration using the method documented in references (Du and Selig 1998, Hansen 2014, Leishman and Beddoes 1989, Viterna and Janetzke 1982). Fig. 2 shows an example of the unprocessed/corrected lift coefficients. Once this information was prepared, the FAST-AeroDyn simulation was carried out with parameter settings described previously in this section

2.2 Aeroelastic-aerodynamic simulation results

By using the FAST and AeroDyn together, a time marching aeroelastic-aerodynamic simulation was performed. For the aerodynamic part, AeroDyn obtains the blade status including the orientation, the linear velocity and angular velocity of each blade element, combining with the imported wind velocity and blade aerodynamic coefficients at each time increment. After that, for each blade element, the axial induction factors are calculated using the iteratively method (Moriarty and Hansen 2005) since they are functions of angle of attack, relative wind angle and corresponding lift and drag aerodynamic coefficients.

Once the induction factors are determined, the relative wind angle, angle of attack and relative wind velocity are calculated using the following equations, respectively (Moriarty and Hansen 2005)

$$\begin{aligned} \varphi &= \tan^{-1} \left(\frac{v_N}{v_T} \right) \\ &= \tan^{-1} \left(\frac{U(1-a) + v_{e-op}}{\Omega r(1+a') + v_{e-ip}} \right) \\ \alpha &= \varphi - \theta_p \end{aligned} \quad (1)$$

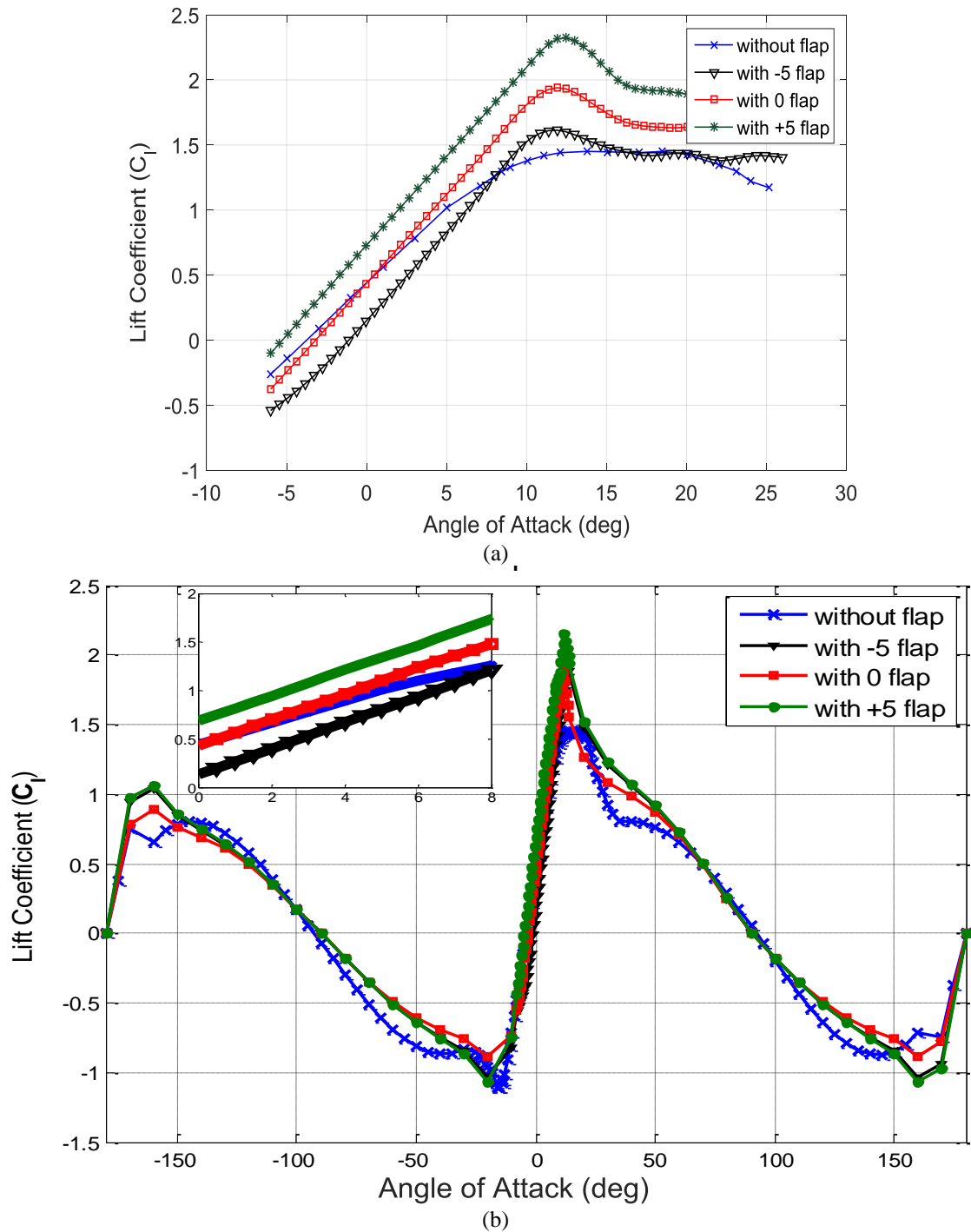


Fig. 2 (a) unprocessed lift coefficients obtained from CFD simulation and (b) corrected lift coefficients after taking 3D effects into consideration and extrapolating to a whole range

where α is the angle of attack; φ is the relative wind angle; θ_p is the blade pitch angle; Ω is the rotor speed in rpm; U is the wind velocity; a , and a' are the axial induction factor and tangential induction factor; v_{e-op} and v_{e-ip} are the element motion velocity out the rotation plane and in the rotation plane, respectively; r is the radial location of the blade section.

To this point, all the local flow information related to the characterization of the boundary layer profile has been obtained.

After running the FAST-AeroDyn simulation, the aerodynamic information can be extracted at the blade-flap section at 59 m radial location (90% blade), as well as the time variations of angle of attack (Fig. 3(a)) and axial induction factor (Fig. 3(b)). The plots started at 30 seconds

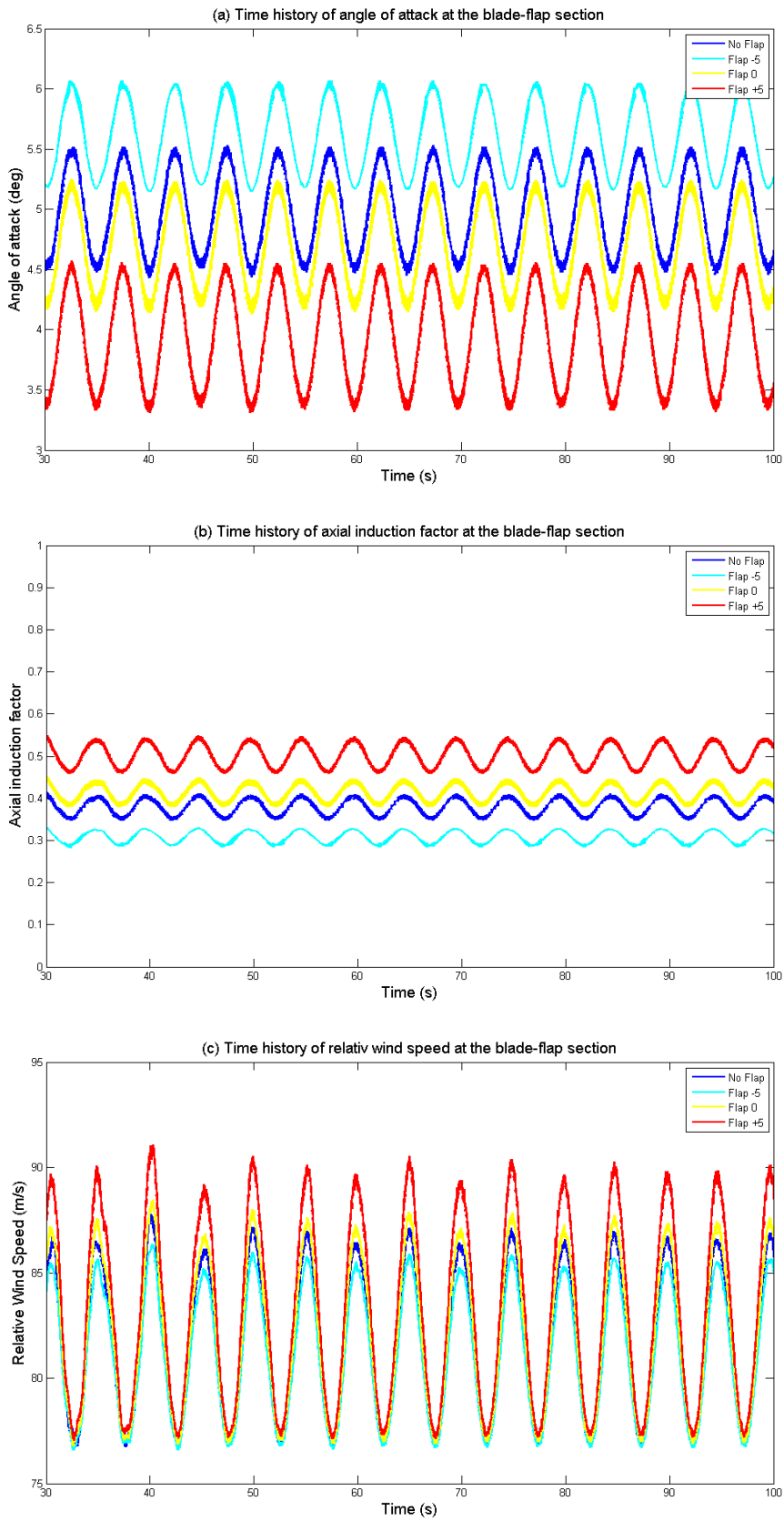


Fig. 3 AeroDyn time history output of (a) angle of attack, (b) axial induction factor and (c) relative wind speed at the blade-flap section

to avoid confusing results caused by the start-up transient, and ended at 100 seconds to avoid redundant results since the results are almost perfectly periodic. From Fig. 3(a), the angle of attack decreases with increasing flap angle and the blade without flap has smaller angle of attack than the one with -5° flap. On the contrary, according to Fig. 3(b), the axial induction factor increases with increasing flap angle and the blade without flap has larger induction factor than the one with -5° flap. The results are reasonable since the relative wind angle is equal to angle of attack for this simulation case due to no blade pitch control setting. The angle of attack is inversely proportional to the axial induction factor, as shown below

$$\alpha = \tan^{-1} \left(\frac{U(1-a) + v_{e-op}}{\Omega r(1+a') + v_{e-ip}} \right) \quad (2)$$

Therefore, the trends in Figs. 3(a) and 3(b) should be opposite. For the same angle of attack, according a simplified equation (Manwell *et al.* 2010)

$$a = \left(1 + \frac{4 \sin^2 \varphi}{\sigma' C_l \cos \varphi} \right)^{-1} \quad (3)$$

The axial induction factor is directly proportional to the lift coefficient. According the CFD simulation result for angle of attack ranging from $0\sim 8^\circ$, the lift coefficients increase with increasing flap angle (magnified view in Fig. 2). The blade without flaps has larger lift coefficient than the one with a -5° flap. Hence the axial induction factor of blade without flaps should be larger than the one with a -5° flap. To this point, Figs. 3(a) and 3(b) are validated. The relative wind speed U_{rel} can be readily calculated using Eq. (4), plotted as Fig. 3(c).

$$U_{rel} = \frac{U(1-a)}{\sin \varphi} \quad (4)$$

The relative wind speed increases with increasing flap angle and the blade without flap has larger relative wind speed than the one with -5° flap.

3. Boundary layer velocity profile characterization

3.1 Interpolation based on the CFD simulation results and AeroDyn time variations

Both the aerodynamic coefficients and the velocity contour for different angle of attacks were obtained from the results of CFD simulations. In order to plot the velocity profile within the boundary layer around the airfoil, the following steps were taken. For a particular angle of attack, the non-dimensionalized CFD results were firstly transferred to a postprocessor ParaView (Henderson 2007). The reason is that the velocity along a specified line can be easily reported using ParaView.

After that, 14 critical locations (10 locations for the blade without flap) were preselected at the top and bottom surfaces of the blade and flap as possible locations for sensor installations, in order to capture the flow pattern and boundary velocity profile (Fig. 1). In the next step, the normal directions were calculated based on the sensor locations. The corresponding normal line starting from the sensor location was defined in ParaView and the velocity values along this line were obtained using ParaView. However, the directly reported velocity value was with respect to the global coordinates, which were subsequently transformed into the local coordinate system whose y axis coincides with the specified normal line. After these steps, the velocities perpendicular to the defined line were obtained.

The process described above was carried out for four different blade-flap combinations (blade without flap, blade with -5° , 0° , and $+5^\circ$ flap) at four different angle of attacks ($+2^\circ$, $+4^\circ$, $+6^\circ$, and $+8^\circ$), resulting in a boundary velocity profile data base. At one particular time step, one can find the instantaneous angle of attack and perform an interpolation using the data base to get the current boundary layer velocity profile at the 14 proposed locations for sensors (as indicated in Fig. 1). For example, at $t = 35$ seconds, the angle of attacks are 4.53° for Case 1. Using the Lagrange interpolating polynomial, the non-dimensionalized boundary layer velocity profiles were plotted in Fig. 4. It needs to point out that the local maximum velocities of the five sensor locations on the blade's top surface are all larger than the non-dimensionalized inlet velocity, which is 1 m/s. On the contrary, the local maximum velocities of the five sensor locations on the blade's bottom surface are all smaller than 1 m/s. This is due to the influence of the pressure gradient around the airfoil. The pressure on the top surface is smaller than the bottom surface. According to Bernoulli's equation, the velocity on the top surface should be larger than the velocity on the bottom surface. In addition, Fig. 4 clearly shows the transition from laminar boundary layer flow to the turbulent boundary layer flow from the leading edge to the trailing edge.

3.2 Boundary layer thickness and velocity profile variation with time

As discussed above, for each time step, a boundary velocity profile can be obtained. Usually, the boundary layer thickness δ is defined as the distance y across the boundary layer from the boundary to the point where the velocity $v(y)$ has reached 99% of the free stream velocity v_{inf} , expressed as

$$\delta = y @ (v(y) = 0.99v_{inf}) \quad (5)$$

However, due to the pressure gradient's influence, the free stream velocity here was replaced by the local free stream velocity once it has approached a constant value. In this way, the boundary layer thickness can be calculated for each proposed sensor location to provide reference information for fluid sensor deployment.

(Case 1).

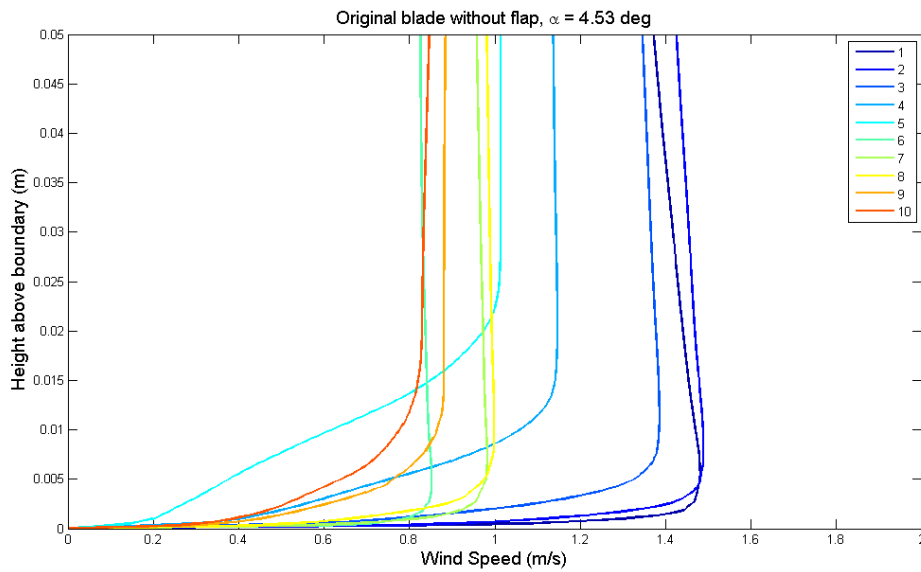


Fig. 4 Non-dimensionalized boundary layer velocity profiles of 10 possible sensor locations

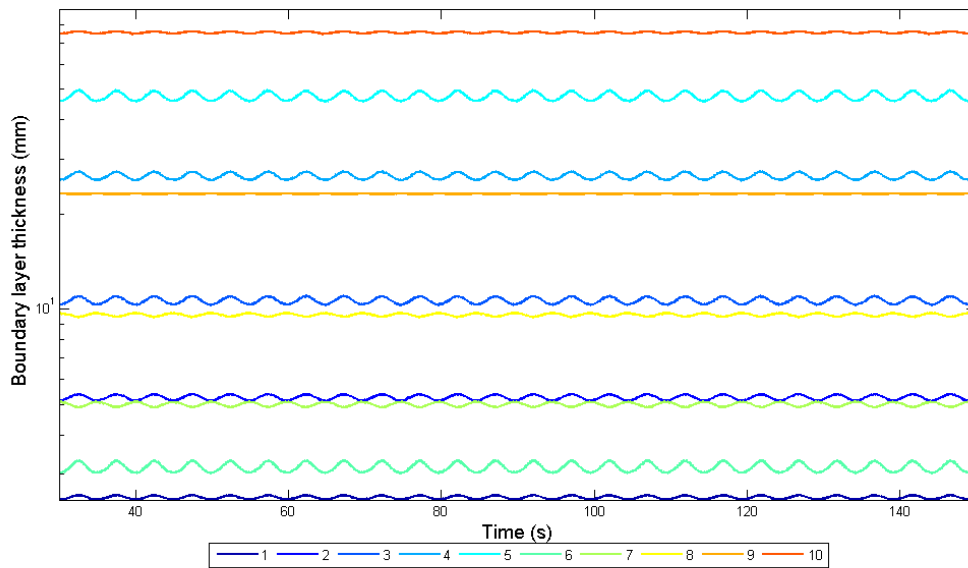


Fig. 5 Time variation of boundary layer thickness at different possible sensor locations

From Figs. 3(a) and 3(c), the time-marching FAST-AeroDyn simulation provides the time variations of angle of attack and relative wind speed. By repeating the procedures for each time increment, the boundary layer velocity profile as well as the thickness variation with time can be obtained.

To obtain the actual boundary layer thickness, the non-dimensionalized thickness was multiplied with the actual chord length of the blade section, which is 2 m. Similarly, to obtain the actual boundary layer velocity magnitude, the non-dimensionalized velocity was multiplied with the actual relative wind speed, which has been obtained as Fig. 3(c).

Fig. 5 shows the time variations of boundary layer thickness of the blade at different proposed sensor locations

The y axis is in logarithmic scale. From a sensor design stand point, the boundary layer thicknesses of the possible sensor locations are less than 17 mm. It should be noted that the boundary layer thickness at location 4, 5, 9 and 10 are larger than the others. This is because these locations are close to the trailing edge, where flow separation tends to occur. The performance of hair flow sensor installed at those spots might be less effective. The analysis of the boundary layer thickness provide the following guidance for the sensor design criteria: firstly, the sensor's length should be in the magnitude similar to the boundary layer thickness in order to capture the velocity distribution in the boundary layer; secondly, the proposed locations for sensor

installation should provide high sensitivity to map the behavior of flow field along the blade.

4. Bio-inspired hair cell sensor design

4.1 Anatomy structure of hair cell as source of bio-inspiration

The previous analysis identified the characteristics of flow boundary layer in light of the turbine blade structure. It also provided the guidance on the flow sensor design (i.e., the dimension, sensitivity requirements, etc.) as well as spatial placement. A bio-inspired hair cell sensor was proposed to sense the flow field at critical locations along the blade. The hair sensors in the lateral line of aquatics, commonly known as neuromasts, provides flow sensing with direction sensitivity due to the unique staircase structure of the hair cells (van Netten 2006). The neuromasts are composed of receptor cells called hair cells. A number of hair cells are encapsulated in a gelatinous cupula, which directly interact with surrounding fluid. The displacements due to the flow will cause changes of the firing rate of afferent fibers connected to the hair cells. The overall directional sensitivity of a neuromast follows a cosine function (Flock 1965, Jürgen Berger 1998).

Inspired by the function and structure of the hair cell, an artificial hair sensor was designed to emulate the directional sensitivity of the hair cell of fish (Tao *et al.* 2013). The transduction function is realized by utilizing the piezoelectric microfibers as the sensing element and the directional sensitivity is achieved by patterning the electrodes on the fibers. The piezoelectric microfiber serves not only as the shaft mimicking the biological hair sensors, but also as the transduction element which converts external stimulations to electrical signals (Fig. 6(a)). When a piezoelectric fiber is stimulated by a fluid induced pressure variations or acoustic waves, the deformation of the fiber produces charges on the surface (due to the piezoelectric effect). Electrical charges with different polarities concentrate on different areas depending on the nature of strains (i.e., tensile or compressive); this results in an electrical potential difference. Through the pair of electrodes, this electrical potential difference can be measured and recorded. The gap between the two electrodes prevents electric neutralization and ensures the directional sensitivity. The output voltage from the sensor varies with the direction of load with a cosine function, which is also the directional sensing characteristic of the hair cells in fish.

A drawback of the design is that the naked piezoelectric fiber is brittle in nature. Further inspired by the structure of the fish superficial neuromast, in which the hair cells are encapsulated with compliant cupula, the durability of the piezoelectric hair sensor is improved by embedding the piezoelectric microfiber in a host material (Fig. 6(b)). To achieve best performance of the sensor, this analysis aims at answering two questions: 1) what's the optimal geometry of the sensor? 2) what type of material should be selected for the host material? An in-depth analysis of the response of the sensor is required to answer these questions.

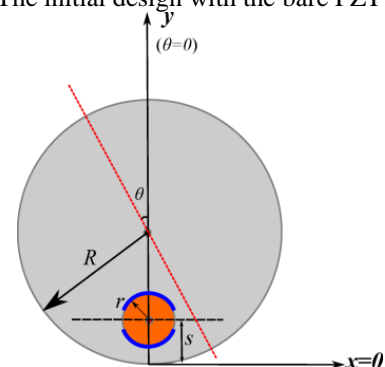
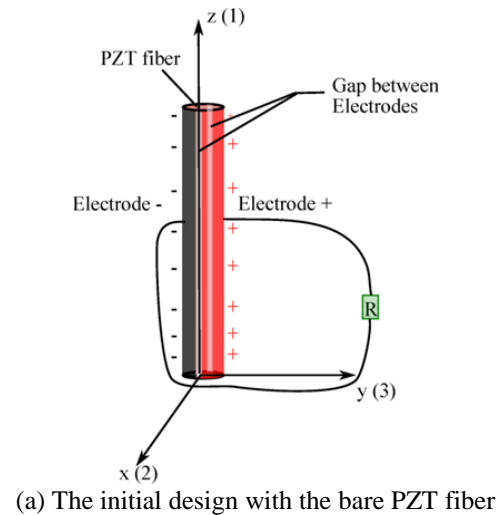


Fig. 6 The design of the hair sensor: R , r , and s are the diameter of the host cylinder, the diameter of the microfiber, and the distance between the center of microfiber and the host material, respectively

To answer these questions, the governing parameters and their influences on the performance of the sensor were studied with a simplified analytical model; the sensitivity of the sensor was also modeled numerically with a fully-coupled model with the assistance of computer simulation, which considered the complex geometry of the composite sensor, the unique pattern of the electrodes, and the mechano-electrical coupling process.

4.2 Model and optimization of artificial hair cell design

The goal of artificial hair flow sensor is to have directivity in responses similar to the hair cells in fish (Eq. (6)).

$$V(\theta) = V_{\theta=0} \cdot \cos \theta \quad (6)$$

The sensitivity of the sensor (S) is defined as the ratio between the output voltage at the zero degree direction ($V(\theta)=0$) and the applied force (F): $S = \frac{V_{\theta=0}}{F}$. An important goal of sensor design is to achieve the desirable mechanical and electrical impedance match. A sensitivity

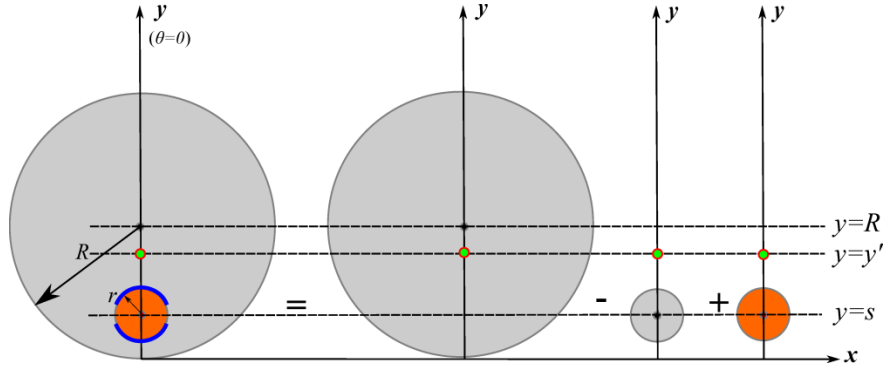


Fig. 7 Equivalent components of the composite sensor

analysis was conducted using an analytic model, which is further validated with FEM analysis.

4.2.1 Analytical model

To describe the sensor's response with an analytic model, the composite hair cell element was assumed to be subjected to a constant force (F) at the top at the direction of $\theta=0$, which was defined following the angle convention as illustrated in Fig. 6(b). To determine the location of the neutral axis when the sensor is bended, the composite sensor can be treated as the combination of three independent components (Fig. 7).

These three components are: 1) a "positive" complete cylinder with radius R , of the host material, 2) a "negative" cylinder with radius r , of the host material, at the location of $y=s$, $x=0$, and 3) a "positive" cylinder with radius r , of the piezoelectric material, at the location of $y=s$, $x=0$. The neutral axis was assumed located at $y=y'$, with the reference $y=0$ as shown in Fig. 7.

The modulus of the host material was assumed to be smaller than that of the piezoelectric fiber; therefore the neutral axis was located in the lower half of the sensor (Fig. 7). Assuming that the structure is in pure bending mode, the location of the neutral axis can be determined as Eq. (7). In Eq. (7), E_h and E_p are the elastic moduli of the host material and the piezoelectric fiber, respectively; A_h and A_p are the cross-section areas of the complete host cylinder and the piezoelectric fiber, respectively; y' , y_h , y_p are the location of the neutral axis, the locations of the centroids of the complete host cylinder and the piezoelectric fiber, respectively.

$$y' = \frac{E_h A_h y_h - E_h A_p y_p + E_p A_p y_p}{E_h A_h - E_h A_p + E_p A_p} \quad (7)$$

Set $\frac{R}{r} = n$, $\frac{s}{r} = \mu$, and $\frac{E_p}{E_h} = \eta$. The location of the

neutral axis of the composite sensor can be non-dimensionalized as shown in Eq. (8).

$$y' = \frac{n^3 + (\eta - 1)\mu}{n^2 + (\eta - 1)} \cdot r \quad (8)$$

The average strain at the centroid line of the piezoelectric fiber is the integration of the strain at the fiber's centroid along the whole length of the sensor (Eq. (9)). In Eq. (9), L is the length of the sensor; \overline{EI} is the equivalent stiffness of the composite sensor, which can be calculated using Eq. (10) or its dimensionless form, Eq. (11). Plug Eq. (11) into Eq. (9). The average strain on the centroid line of the piezoelectric fiber is obtained as Eq. (12)

$$\varepsilon_{centroid} = \frac{\int_0^L \frac{F \cdot (L-z)}{\overline{EI}} \cdot (y-y') \Big|_{y=s} dz}{L} \quad (9)$$

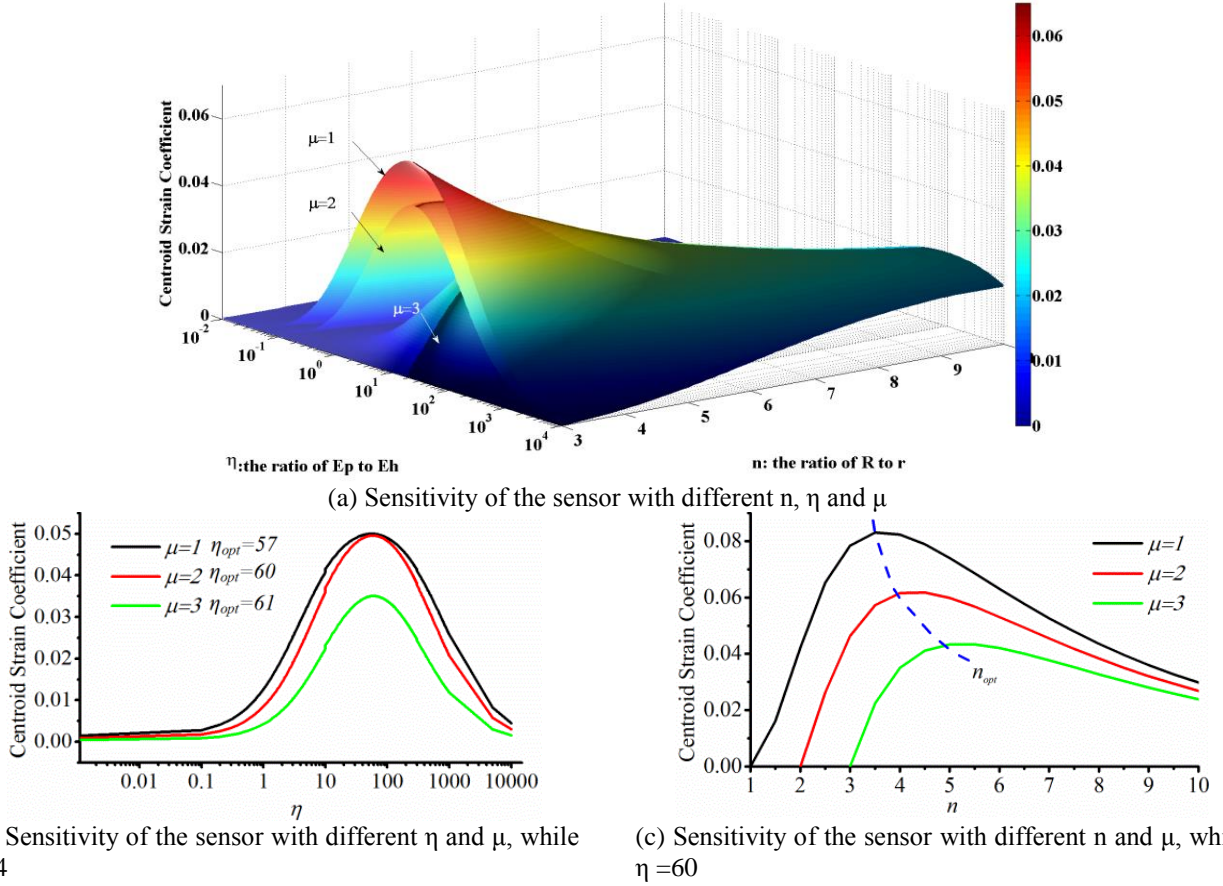
Eq. (12) clearly indicates that the average strain on the centroid line of the piezoelectric fiber is linearly dependent on the applied load (F) and the length of the sensor (L). The second term in Eq. (12) is considered as the centroid strain coefficient, which describes the influence of configurations of the composite sensor on the bending of the sensor. The parameters include the radius ratio of the host material to the piezoelectric fiber (n) and the radius of the piezoelectric fiber (r), the modulus ratio of the piezoelectric fiber to host material (η) and the eccentricity of the piezoelectric material $(n-\mu)r$. The centroid strain coefficient is plotted in Fig. 8, from which the influence of each parameter (n , η , μ) can be evaluated.

$$\overline{EI} = E_h [I_h + (R-z')^2 \pi R^2] - E_h [I_p + (z'-s)^2 \pi r^2] + E_p [I_p + (z'-s)^2 \pi r^2] \quad (10)$$

$$\overline{EI} = E_h \frac{\pi r^4}{4} \cdot \left[n^4 + \eta - 1 + 4n^2 (\eta - 1) \frac{(n-\mu)^2}{n^2 + (\eta - 1)} \right] \quad (11)$$

$$\varepsilon_{centroid} = \left(\frac{2F \cdot L}{E_p \pi r^3} \right) \cdot \left[\frac{\eta \cdot n^2 (n-\mu)}{(n^4 + \eta - 1)(n^2 + \eta - 1) + 4n^2 (\eta - 1)(n-\mu)^2} \right] \quad (12)$$

With increasing relative eccentricity (μ) of the piezoelectric fiber, the coefficient also increases for the same diameter ratio n and modulus ratio η ; given a certain eccentricity, the coefficient surface defined by both n and η is hump-shaped (Fig. 8(a)); the coefficient with same n values and increasing η values follows an increasing-then-

Fig. 8 Sensor sensitivity analysis with different n , η , and μ

decreasing fashion and the optimal η values to achieve the highest coefficient become slightly larger for increasing μ values (Fig. 8(b)); the coefficient with same η values and increasing n values also follows an increasing-then-decreasing fashion and the optimal n values to achieve the highest coefficient become larger for increasing μ values (Fig. 8(c)). Overall, the changing of the centroid strain coefficient with the governing parameters is not only nonlinear, but also non-monotonic.

Therefore, the sensitivity of the sensor is determined by both the geometry and mechanical properties of the sensor components. To achieve certain sensitivity, there are different combinations of geometries and mechanical properties. For example, if the geometry of the sensor is fixed due to the fabrication limits, the optimal host material to achieve highest sensitivity can be determined by calculating its elastic modulus; an easy method to obtain the optimal value for η is by setting $\frac{\partial \varepsilon_{centroid}}{\partial \eta} = 0$ (e.g., $\eta_{opt} = 117.26$ when $n=5$ and $\mu=1.5$). On the other hand, if the available materials are limited, one can determine the geometry of the composite sensor to achieve certain sensitivity.

4.2.2 Finite element analysis

In the analytical model described in the previous section, only one loading condition was studied, that was, a

constant load in the direction of $\theta=0$. The linearity of the sensor in this direction can be explained with Eq. (12). However, the analytical expression for the elastic strain in other directions has not been derived due to the non-symmetry nature of the sensor, which results in different equivalent stiffnesses and different neutral surfaces with external load with different directions. Therefore, the linearity and the directionality of the sensor are not validated directly. Furthermore, the output voltage of the sensor was assumed to be linearly proportional to the average strain on the centroid line of the PZT fiber. And this assumption needs further validation.

To further analyze the sensor performance, a fully coupled piezoelectric model was employed to study both the mechanical and the electrical responses of the sensor. Using Cartesian tensor notation, the governing equations for the fully coupled model are shown in Eq. (13). In Eq. (13), S_{ij} and T_{kl} is the mechanical strain and stress tensor, respectively; D_i and E_k is the electric displacement and electric field, respectively; s_{ijkl}^E is the elastic compliance tensor in condition of constant electric field and ε_{ik}^T is the dielectric permittivity in condition of constant stress status; and d_{kij} and d_{ikl} are the piezoelectric coefficient matrices.

$$\begin{cases} S_{ij} = s_{ijkl}^E T_{kl} + d_{kij} E_k \\ D_i = \varepsilon_{ik}^T E_k + d_{ikl} T_{kl} \end{cases} \quad (13)$$

Table 1 Properties of PZT 5H

Parameter	Value	Note
Elastic compliance matrix	$s^E = \begin{bmatrix} 16.5 & -4.78 & -8.45 & 0 & 0 & 0 \\ -4.78 & 16.5 & -8.45 & 0 & 0 & 0 \\ -8.45 & -8.45 & 20.7 & 0 & 0 & 0 \\ 0 & 0 & 0 & 43.5 & 0 & 0 \\ 0 & 0 & 0 & 0 & 43.5 & 0 \\ 0 & 0 & 0 & 0 & 0 & 42.6 \end{bmatrix} \times 10^{-12} 1/Pa$	Note that, following IEEE standard 176-1987, tensor indices ij and kl is replaced with p and q , respectively, with i, j, k, l taking the values 1, 2 and 3 and p, q taking values of 1, 2, 3, 4, 5, and 6.
Piezoelectric coupling matrix	$d = \begin{bmatrix} 0 & 0 & 0 & 0 & 741 & 0 \\ 0 & 0 & 0 & 741 & 0 & 0 \\ -274 & -274 & 593 & 0 & 0 & 0 \end{bmatrix} \times 10^{-12} C/N$	
Permittivity matrix	$\epsilon^T = \begin{bmatrix} 3130 & 0 & 0 \\ 0 & 3130 & 0 \\ 0 & 0 & 3400 \end{bmatrix} \times \epsilon_0$	ϵ_0 is the permittivity of vacuum, or, 8.85×10^{-12} F/m.

The fully coupled equations (Eq. (13)) were solved using finite element method (FEM) in COMSOL®. The geometry of the sensor was fixed in the FEM models to focus on the influence of external loads and the modulus of the host material on the performance of the sensor. The diameter of the PZT fiber was assumed to be $10\mu\text{m}$, the diameter of the host cylinder was assumed to be $50\mu\text{m}$, and the length of the composite sensor was assumed to be 1mm (note: the length of sensing element can be different from the wind catching structure which is solely a structural element and can be in 10s of mm). These parameters were chosen to mimic the length scale of the neuromasts in fish.

The hair structure is modeled as a cantilever as shown in Fig. 6(a), just like the neuromast of fish. Therefore, one end of the sensor was fixed and the other end is free to move; the loading is a concentrated point force applied at the free end of the cantilever. The loading point is located at the location with a coordinate of the loading point is $x=0, y=0$ and $z=1\text{mm}$ (Point A in Fig. 6(b)). The mechanical contact between the piezoelectric material and the host material is considered as full contact which means that the stress and strain at the interface is shared by two materials. This is realized by assigning a boundary condition of “symmetry” at the interface.

The electrical boundary conditions of the inner-side and outer-side electrode are floating potential and ground, respectively (Fig. 9). Therefore the electric potential of the outer-side electrode was kept as zero and the electric potential of the other electrode was determined by calculating the potential difference between the two electrodes based on Eq. (13).

The material of the piezoelectric fiber was assumed to be PZT 5H and the modulus of the host material was defined by $E_h = \eta \cdot E_p$, and η changed from 10^{-2} to 10^4 . The mechanical, piezoelectric coupling and dielectric properties of PZT 5H are listed below.

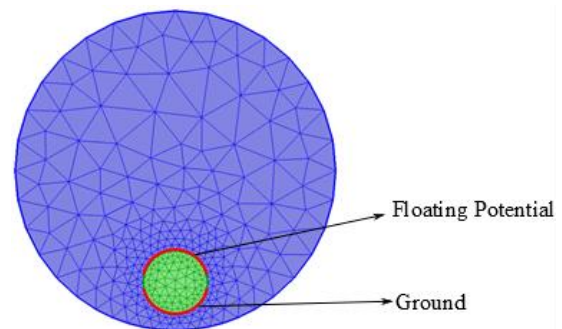


Fig. 9 The meshed domains and the electrical boundary conditions

The domains were meshed with tetrahedral elements; the mesh size of the PZT domain was fine enough to make sure that there were at least three layers of elements in the “gap” region between the two electrodes (Fig. 9) and this treatment was to ensure the resolution of stress field in this region.

The linearity of the sensor in a particular loading direction was validated via a sensitivity study that determines the responses of the piezoelectric hair sensing element to the magnitude of displacement in its free end (Fig. 10(a)). The average centroid strain in the PZT fiber increased linearly with the magnitude of the external excitation (in Fig. 10(a), the deflection was in the direction of $\theta=0$); furthermore, the output voltage of the sensor was indeed linearly dependent on the average centroid strain. The directivity of the sensor was studied by altering the directions of the sensor deflection (Fig. 10(b)). It was validated that with the PZT fiber embedded in the host material eccentrically, the output voltage of sensor still depended on the loading direction with a cosine function, which is the same with the directivity of the bare PZT fiber sensor (Tao *et al.* 2013) and hair cells in neuromasts (Coombes 2001).

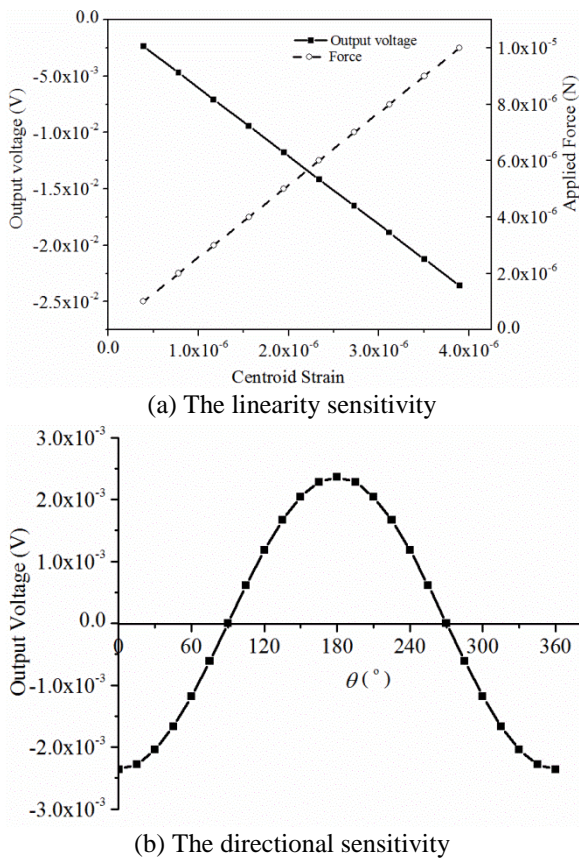


Fig. 10 The linearity and the direction sensitivity of the sensor

The neutral axis locations in the composite sensor with different host materials (i.e., different E_h or η values) were determined using the FEM model; and the results were compared with those calculated using the analytical pure mechanical model; an additional FEM based pure mechanical model was also built to validate the analytical model. The neutral axis locations determined by these three approaches are plotted in Fig. 11(a).

Fig. 11(a) shows that the neutral axis locations with different η values predicted by three methods were consistent with each other; it validated the efficiency of the simplified analytical model, which is more convenient to study the influence of each parameter on the performance of the sensor (Fig. 11). As η increased, the neutral axis moved towards the centroid of the fiber. For example, two representative locations are illustrated in Fig. 11(a); when η is extremely large or the stiffness of the sensor is mainly determined by the PZT fiber, the neutral axis is approximately located at A (i.e., the centroid line of the PZT fiber); when η is 1 or E_p and E_h is equivalent, the neutral axis is located at C (i.e., the centroid line of the composite sensor).

It can also be observed that although very small, there was a discrepancy between the FEM based pure mechanical model and the fully coupled model. For example, the predicted neutral axis locations by the fully coupled model are slightly lower than those predicted by the pure

mechanical model. This is caused by the coupling between the mechanical field and the electrical field (Eq. (13)). The deformation induced electric field tends to “oppose” such deformation and thus makes the PZT fiber slightly “stiffer”.

Therefore, the neutral axis locations based on the coupled model were slightly closer to the PZT fiber.

Fig. 11(b) shows the calculated average strain on the centroid line of the PZT fiber. From Fig. 11(b), the optimal value of η determined by the coupled model for the highest sensitivity was 117, which is almost identical to that predicted using Eq. (12). In practice, the material with modulus of the exact optimal value may not exist; therefore we defined an acceptable modulus range, which covers all the η values between 95% η_{opt} and 100% η_{opt} . This range can be determined from Fig. 11(b), which was 46~300. It can be also observed that the calculated strain based on the coupled model was slightly lower than that predicted based on the pure mechanical FEM model. This is another evidence for the fact that the apparent stiffness of the PZT fiber is stiffer when the piezoelectric effect is considered. Compared with Fig. 11(a), another interesting observation is that when the sensor achieved the highest sensitivity, the neutral axis was lower than B, which is on the intersection line of the AC plane and the surface of the PZT fiber. That is to say, it is “inside” the PZT fiber, or, the entire PZT fiber is not in a pure tension or pure compression state.

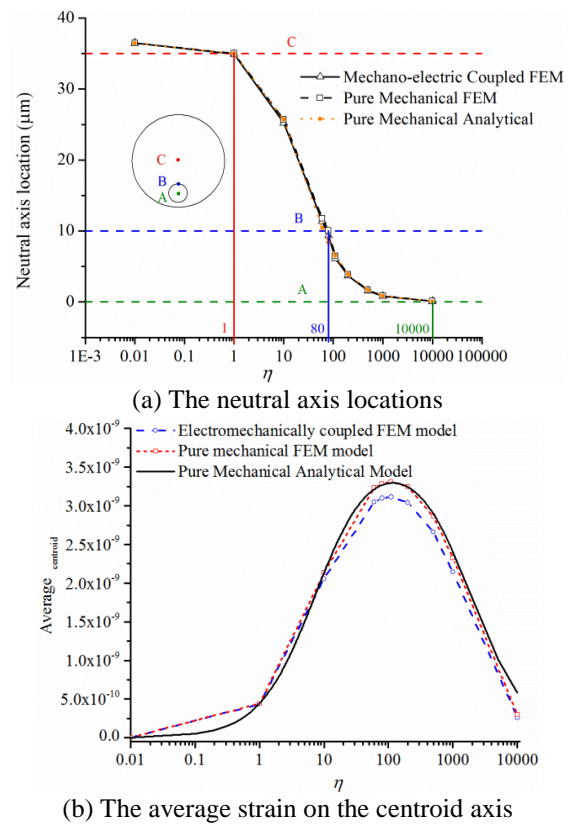


Fig. 11 The calculated neutral axis location and the average strain on the centroid axis for different host materials with different models

The results in this section underscore the importance of the matching between the piezoelectric material and the host material (artificial cupula) in terms of both geometrical and mechanical properties. The simplified mechanical model (Eq. (12)) can be used to estimate the optimal design parameters (n , μ , η) due to its simplicity and relatively high accuracy; to determine the sensitivity of the sensor more accurately, the fully coupled FEM model is needed to account for the coupled piezoelectric effect.

4.3 Prototype hair cell sensor fabrication and preliminary evaluation

A hair cell sensor prototype was fabricated based on the design schema showing in Fig. 12. The transduction element was a piezoelectric fiber with a diameter of $10\ \mu\text{m}$, which was aligned with spiral electrodes for charge collection. Both fiber and spiral supporting structures were encased in a shrinkage tube. The diameter of the shrinkage tube was $50\ \mu\text{m}$, leading to a diameter ratio of $n=5$ between the piezoelectric fiber and the tube. The piezoelectric fiber locates at the outer ring of the tube, leading to a relative eccentricity (μ) of 1. Based on the analysis in 4.2, the host material can be selected considering the optimal modulus ratio η , which is around 100. The Young's modulus of PZT 5H is about 40-60 GPa. Therefore, low-density polyethylene with a Young's modulus of 0.45GPa was selected for the shrinkage tube.

The length of the biomimic hair sensor that captures the mechanical excitation was around 10mm (which can be easily changed depending upon the condition of the boundary layer). To evaluate the sensor's performance, the element was attached to a precise angular controller, which can change the alignment of the sensor from 0° to 360° and display the angle in real-time. The convention for the angle was shown in Fig. 7(b)

As shown in Fig. 12, the sensor was first placed parallel to the scale board and set at a certain orientation (n°). The tip of the sensor was set as the origin and then the tip was bent at fixed distances away from the origin with a pin in n° and $n+180^\circ$. For each alignment, the sensor was released and the vibration induced signals were sampled. For each step, the direction was changed by 15° and three signals for each direction were sampled and the average was used in the following sections. The distances of $\pm 10\ \text{mm}$ and $\pm 15\ \text{mm}$ from the origin were also applied in the directions of 0° , 180° , 90° , and 270° .

A typical signal was in a decaying sine or cosine shape (Fig. 13). The amplitude, frequency, and the polarity of a signal were dependent on the direction of excitation. The absolute value of the first peak (either negative or positive, depending on the direction) represents the amplitude or "strength" of the signal, Fig. 13 shows the amplitude varied with angle. Fig. 14 shows the output voltage was nearly linearly dependent on the deflection of the hair sensor. Fig. 15 shows the output followed a cosine variation with direction of sensor excitation. The directional variation was consistent with what was observed (a cosine variation with angle) in the sensory responses of biological hair cell (Eq. (6) or (Bleckmann 2008)).

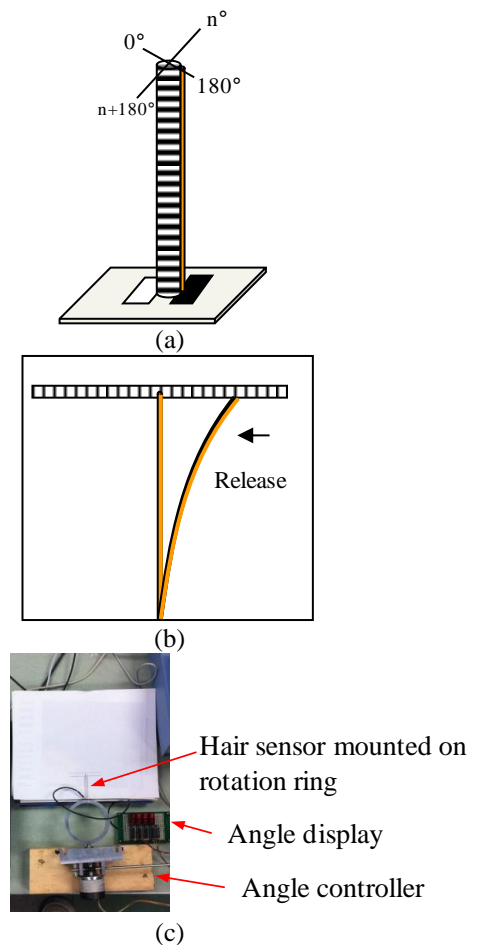


Fig. 12 (a) Convention of orientation of the sensor, (b) illustration of the procedure and (c) laboratory setup

The analyses and experiments verified that the bio-inspired hair sensor element possesses the characteristics of the natural hair flow sensors, the neuromasts. It features good linearity and directional sensitivity. The length of the hair cell sensor will be further optimized based on the predicted boundary layer conditions.

4.4 Flow velocity mapping of hair cell sensors

The experiment on the prototype hair cell sensor established relationships among the sensor tip displacement, deflection direction and output voltage signal. The hair cell sensors are lightweight so that they are not able to alternate the flow pattern and are very sensitive to the change of flow direction and magnitude. Therefore, it is theoretically feasible to apply the hair flow sensor to obtain the flow information. The conventional tufts should be used in conjunction with image techniques to capture their deflected pattern to study the flow. However, it is difficult to photograph them at a far distance or at a high speed due to their small sizes and low visibility. With the development of the hair flow, the flow direction can be obtained by analyzing the collected electrical signals when photographing is not applicable.

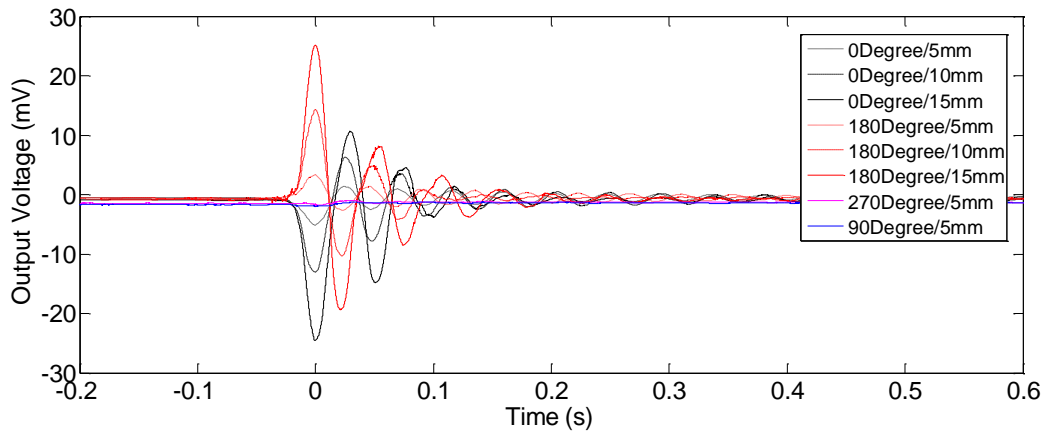


Fig. 13 Signals for different orientations and different initial tip displacements

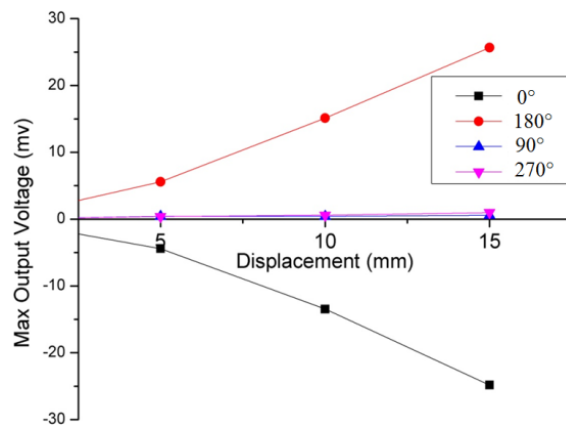


Fig. 14 Near linear relationship between the maximum output voltage and the initial tip displacement

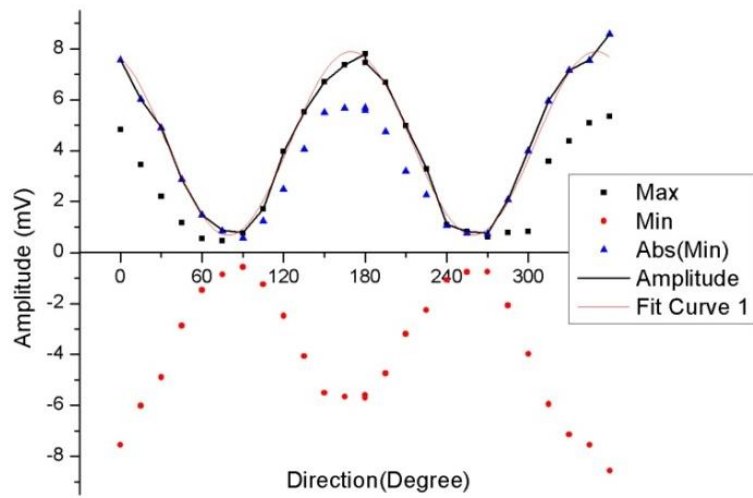


Fig. 15 The characteristics of sensor output voltage to excitation at different directions

The hair cell sensors can be applied in array for flow velocity mapping purpose and the schematic is shown in Fig. 16. Subjected to a turbulent flow, the sensors bend due to the dynamic pressure of the coming flow. The array arrangement makes them spatially coded. The spatial arrangement causes time lags for turbulent events to propagate to different sensors. Using the numbering in Fig. 16(b), the speed, V , and direction of turbulent flow, θ , can be calculated (Yu *et al.* 2010)

$$V = \frac{a}{\sqrt{t_{43}^2 + t_{13}^2}} \quad (14)$$

$$\tan(\theta - 45^\circ) = \frac{\Delta t_{13}}{\Delta t_{43}} \quad (15)$$

where a is the distance between the sensors; Δt_{43} is the time lag between when the flow arrives at Sensor 4 (t_4) and Sensor 3 (t_3); Δt_{13} is the time lag between when the flow arrives at sensor 1 (t_1) and sensor 3 (t_3). By using of a dense array of sensors, the spatial distribution of the turbulence flow velocity can be determined.

A laboratory test was conducted to test this idea. Two hair sensors were aligned in tandem in the same direction and exposed to air bursts produced by a calibrated syringe. The syringe was well-controlled to introduce air burst with velocity of 16 m/s, 12 m/s, 8.5 m/s and 5.5 m/s. The burst traveled to the two sensors and caused them to vibrate. The distances of the two hair sensors varied from 50 mm to 200mm with steps of 50 mm. Examples of measured signals from the two sensors with different spacing are illustrated in Fig. 17(a). A time delay was observed between the two sensor responses and the time delay increased with the spacing of the pair of sensors. Similar to the lateral line system of fish (Chagnaud *et al.* 2008a, Chagnaud *et al.* 2008b), the velocity of burst propagation can be calculated using Eq. (14)

The time delays determined from analyzing the time responses were plotted versus the spacing between the two hair sensors (Fig. 17(b)). It can be concluded that the time delays increased linearly with hair sensor spacing. The calculated velocities of air burst were 15.45 m/s, 11.65 m/s, 8.5 m/s, and 5.5 m/s, respectively. It is concluded that the error of calculated velocities falls within 1.5%~3.5% of the controlled burst velocities, which was monitored by a hot wire thermo-anemometer from EXTECH®, Model 407123. This conceptual experiment proved that the proposed hair sensor has the potential to sense flow speed.

However, there are some challenges at this stage. Although the hair cell sensor can be utilized as an array and the boundary velocity might be calculated by the proposed method, the flow around a typical blade of large scale wind turbines is highly turbulent, which means the sensor will definitely be disturbed by vortex structures of various scales and frequencies brought into the turbulent boundary layer. As a result, such a mathematic scheme needs to be further validated via model and field testing program. A threefold research task is proposed and will be conducted continuously in the future: 1) to scale the prototype hair cell sensor to a proper dimension such that it

can be applied to the wind turbine blade for laboratory and field testing and validation; 2) to study the dynamic behaviors of the hair cell sensor and sensor arrays under turbulence flow; 3) to validate the mathematical model for sensor performance and flow field mapping by conducting field testing under turbulence flow conditions.

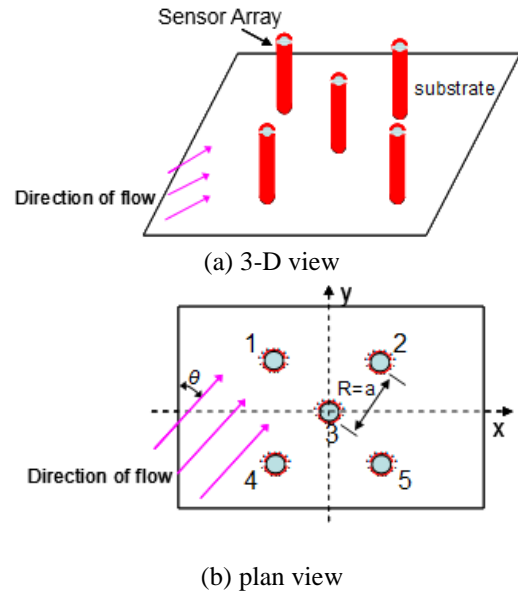


Fig. 16 Schematic of sensor array

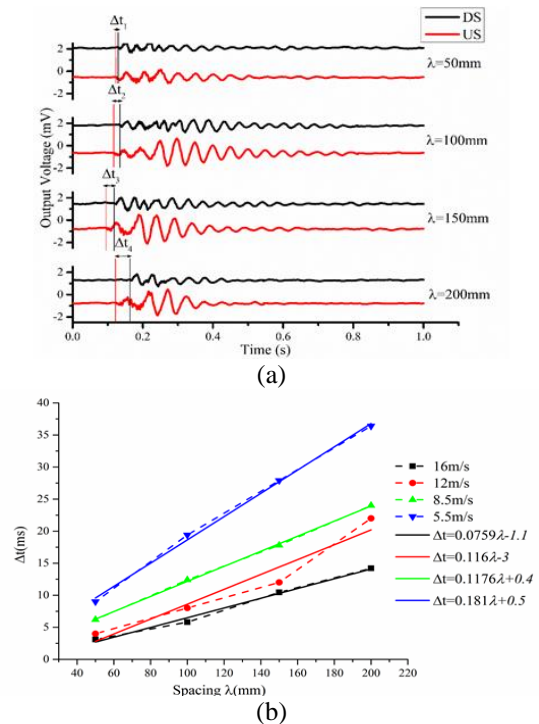


Fig. 17 (a) The measured response signals from two hair sensors aligned with different spacing subjected to burst-induced air flows (the hair sensor in the upstream of the burst is noted as “US” and the one in downstream as “DS”) and (b) the relationship between the spacing of the two hair sensors and corresponding measured time delay

5. Conclusions

A bio-inspired flow sensor is proposed in this study and will be integrated into wind turbine blades in the future to provide input for active flap controllers to mitigate the vibration of the blade structure. Aeroelastic-aerodynamic simulation and CFD simulations are firstly conducted to characterize the boundary layer velocity profile and variation of boundary layer thickness with time at different locations along the blade. The results provide important criteria for the design and placement of flow sensors. Strategies for bio-inspired hair flow sensors and flow field mapping along the wind turbine blade were proposed. The design of hair flow sensor was analyzed with an analytical model as well as a FEM analysis. The performance of a fabricated sensor was experimentally validated, which demonstrated the feasibility of the hair flow sensors in characterizing the boundary velocity and flow direction. The sensor geometry will be further refined based on simulated boundary layer characteristics. The results demonstrate that the proposed sensor has potentials for integration into the blade structure to map the flow field in the real time, which will act as important inputs for the flap control. With the further refinement of sensor design and integration with the flap controller, the long term goal of our research is to construct smart blades with integrated flow sensors and flap control systems. Further experimental testing and validation are necessary to gauge the potentials.

Acknowledgements

The authors gratefully acknowledge the financial support of National Science Foundation under grants 1300970 and 1300149. Since the theory manual of FAST is not officially published, the authors would like to sincerely thank Dr. Jason Jonkman at NREL for kindly providing the manuscript of the manual.

References

- Abbott, I.H. and Von Doenhoff, A.E. (1959), *Theory of wing sections, including a summary of airfoil data*, Moneola, NY: Dover Publications, Inc.
- ANSYS® Academic Research. (2014), ANSYS FLUENT Theory Guide (Release 14.5). ANSYS, Inc.
- Barlas, A. and Van Kuik, G. (2009), "Aeroelastic modelling and comparison of advanced active flap control concepts for load reduction on the upwind 5MW wind turbine", *Proceedings of the 2009 European Wind Energy conference & Exhibition*, Marseille, France.
- Barlas, T. and Van Kuik, G. (2010), "Review of state of the art in smart rotor control research for wind turbines", *Prog. Aerosp. Sci.*, **46**(1), 1-27.
- Basualdo, S. (2005), "Load alleviation on wind turbine blades using variable airfoil geometry", *Wind Eng.*, **29**, 169-182.
- Berg, J., Barone, M. and Resor, B. (2013), "Field test results from the Sandia SMART rotor", *Proceedings of the 51st AIAA aerospace sciences meeting*. Grapevine, TX.
- Bergami, L., Gaunaa, M., Poulsen, N.K. and Buhl, T. (2013), Adaptive trailing edge flaps for active load alleviation in a smart rotor configuration, *DTU Wind Energy*, DTU Wind Energy.
- Bermúdez, L., Velázquez, A. and Matesanz, A. (2002), "Viscous-inviscid method for the simulation of turbulent unsteady wind turbine airfoil flow", *J. Wind Eng. Ind. Aerod.*, **90**(6), 643-661.
- Bleckmann, H. (1994), Reception of Hydrodynamic Stimuli in Aquatic and Semiaquatic Animals, *Stuttgart: Gustav Fischer*.
- Bleckmann, H. (2008), "Peripheral and central processing of lateral line information", *J. Comp. Physiol. A*, **194**(2), 145-158.
- Bossanyi, E. (1996), GH Bladed theory and user manuals. England: Garrad Hassan and Partners Limited.
- Bredberg, J. (2000), On the wall boundary condition for turbulence models. Report 00/4, Dept. of Thermo and Fluid Dynamics, Chalmers University of Technology, Gothenburg. Also available at www.tfd.chalmers.se/lada.
- Brendel, M. and Mueller, T.J. (1988), "Boundary-layer measurements on an airfoil at low Reynolds numbers", *J. Aircraft*, **25**(7), 612-617.
- Brucker, C., Spatz, J. and Schroder, W. (2005), "Feasibility study of wall shear stress imaging using microstructured surfaces with flexible micropillars", *Exp. Fluids*, **39**(2), 464-474.
- Buhl, T., Bak, C., Gaunaa, M. and Andersen, P.B. (2007), "Load alleviation through adaptive trailing edge control surfaces: ADAPWING overview", *Proceedings of the 2007 European Wind Energy Conference and Exhibition*. Milan, Italy: European Wind Energy Association.
- Buhl, T., Gaunaa, M. and Bak, C. (2005a), "Load reduction potential using airfoils with variable trailing edge geometry", *Proceedings of the 43th AIAA/ASME*, Reno, NV, USA.
- Buhl, T., Gaunaa, M. and Bak, C. (2005b), "Potential load reduction using airfoils with variable trailing edge geometry", *J. Solar Energy Eng.*, **127**(4), 503-516.
- Castagnet, D., Barlas, T., Buhl, T., Poulsen, N.K., Wedel-Heinen, J.J., Olesen, N.A., Bak, C. and Kim, T. (2014), "Full-scale test of trailing edge flaps on a Vestas V27 wind turbine: active load reduction and system identification", *Wind Energy*, **17**(4), 549-564.
- Chagnaud, B.P., Bleckmann, H. and Hofmann, M.H. (2008a), "Lateral line nerve fibers do not code bulk water flow direction in turbulent flow", *Zoology*, **111**(3), 204-217.
- Chagnaud, B.P., Brucker, C., Hofmann, M.H. and Bleckmann H. (2008c), "Measuring flow velocity and flow direction by spatial and temporal analysis of flow fluctuations", *J. Neurosci.*, **28**(17), 4479-4487.
- Coombs, S. (2001), "Smart skins: information processing by lateral line flow sensors", *Auton. Robot.*, **11**(3), 255-261.
- Coombs, S. and Fay, R.R. (1989), "The temporal evolution of masking and frequency selectivity in the goldfish", *J. Acoust. Soc. Am.*, **86**, 925-933.
- Daynes, S. and Weaver, P.M. (2012), "A morphing trailing edge device for a wind turbine", *J. Intel. Mat. Syst. Str.*, 1-11.
- Devinant, P., Laverne, T. and Hureau, J. (2002), "Experimental study of wind-turbine airfoil aerodynamics in high turbulence", *J. Wind Eng. Ind. Aerod.*, **90**, 689-707.
- Du, Z. and Selig, M.S. (1998), A 3-D stall-delay model for horizontal axis wind turbine performance prediction, *AIAA Paper 21*.
- Fisher, D.F. and Meyer, Jr., R.R. (1988), Flow visualization techniques for flight research. *NASA Technical Memorandum 100455*. Edwards, California: National Aeronautics and Space Administration.
- Flock, Å. (1965), "Transducing mechanisms in the lateral line canal organ receptors", *Cold Spring Harbor Symposia on Quantitative Biology*. Cold Spring Harbor Laboratory Press, 133-145.
- Garcia-Sagrado, A. and Hynes, T. (2012), "Wall pressure sources near an airfoil trailing edge under turbulent boundary layers", *J. Fluid. Struct.*, **30**, 3-34.

- Ge, M., Fang, L. and Tian, D. (2015), "Influence of reynolds number on multi-objective aerodynamic design of a wind turbine blade", *PLoS one* 10, e0141848.
- Gillebaart, T., Bernhammer, L., Van Zuijlen, A. and Van Kuik, G. (2014), "Active flap control on an aeroelastic wind turbine airfoil in gust conditions using both a CFD and an engineering model. *J. Physics: Conference Series*. IOP Publishing, 012060.
- Glassmaker, N.J., Jagota, A., Hui, C.Y. and Van Kuik, G (2004), *J. Royal Soc. Interface* 1.
- Gleyzes, C. and Capbern, P. (2003), "Experimental study of two AIRBUS/ONERA airfoils in near stall conditions. Part I: Boundary layers", *Aerosp. Sci. Technol.*, **7**(6), 439-449.
- Hansen, A.C. (2014), AirfoilPrep: An Excel workbook for generating airfoil tables for AeroDyn and WT_Perf. v2.02.03 ed. NWTCC Information Portal (AirfoilPrep). <https://nwtcc.nrel.gov/AirFoilPrep>. Last modified 19-December-2014 ; Accessed 03-April-2015: National Renewable Energy Laboratory.
- Henderson, A. (2007), ParaView Guide, A Parallel Visualization Application. <http://www.paraview.org/>: Kitware Inc.
- Henriksen, L.C., Bergami, L. and Andersen, P.B. (2013), "A model based control methodology combining blade pitch and adaptive trailing edge flaps in a common framework", *Proceedings of the European Wind Energy Association 2013*, Vienna, Austria.
- Jonkman, J.M. (to be published) FAST theory Manual. Golden, CO: National Renewable Energy Laboratory.
- Jonkman, J.M. and Buhl, Jr., M.L. (2005), FAST user's guide. Golden, CO: National Renewable Energy Laboratory.
- Jonkman, J.M., Butterfield, S., Musial, W. and Scott, G. (2009), *Definition of a 5-MW reference wind turbine for offshore system development (NREL/TP-500-38060)*, Golden, CO: National Renewable Energy Lab.
- Jürgen, B. (1998), "Cover image: Cluster of superficial sensory hair cells at the surface of the skin of a larval zebrafish", *Neuron* 20.
- Kooijman, H., Lindenburg, C., Winkelaar, D. (2003), "DOWEC 6 MW Pre-Design: Aero-elastic modeling of the DOWEC 6 MW pre-design in PHATAS. *DOWEC Dutch Offshore Wind Energy Converter 1997-2003 Public Reports*. Petten, Netherlands: Energy Research Center of the Netherlands (ECN).
- Lackner, M.A. and van Kuik, G. (2010), "A comparison of smart rotor control approaches using trailing edge flaps and individual pitch control", *Wind Energy*, **13**(2-3), 117-134.
- Laino, D.J. and Hansen, A.C. (2002), User's guide to the wind turbine aerodynamics computer software AeroDyn. *Windward Engineering, LC, Salt Lake City, UT*.
- Larsen, T.J. and Hansen, A.M. (2007), *How 2 HAWC2, the user's manual*: Risø National Laboratory.
- Leishman, J. and Beddoes, T. (1989), "A semi-empirical model for dynamic stall", *J. Am. Helicopter Soc.*, **34**, 3-17.
- Løgstrup Andersen, T., Aagaard Madsen, H., Barlas, T.K., Mortensen, U.A. and Andersen, P.B. (2015), *Design, manufacturing and testing of Controllable Rubber Trailing Edge Flaps (DTU Vindenergi-E-0076)*: DTU Wind Energy.
- Manwell, J.F., McGowan, J.G. and Rogers, A.L. (2010), *Wind energy explained: theory, design and application*: John Wiley & Sons.
- Marrant, B. and Van Holten, T. (2006), "Comparison of smart rotor blade concepts for large offshore wind turbines", *Offshore Wind Energy and Other Renewable Energies in Mediterranean and European Seas*.
- Menon, M., Ponta, F., Sun, X. and Dai, Q. (2016), "Aerodynamic analysis of flow-control devices for wind turbine applications based on the trailing edge slotted flap concept", *J. Aerospace Eng.*, **29**(5).
- Menter, F.R. (1994), "Two-equation eddy-viscosity turbulence models for engineering applications", *AIAA J.*, **32**, 1598-1605.
- Michael, S., Robert, D. and Gregory, W. (2011), "Wind tunnel testing airfoils at low reynolds numbers", *Proceedings of the 49th AIAA Aerospace Sciences Meeting including the New Horizons Forum and Aerospace Exposition*. American Institute of Aeronautics and Astronautics.
- Montgomery, J., Baker, C.F. and Carton, A.G. (1997), "The lateral line can mediate rheotaxis in fish", *Nature*, **389**, 960-963.
- Moriarty, P.J. and Hansen, A.C. (2005), AeroDyn theory manual. Golden, Colorado, USA: National Renewable Energy Laboratory
- Ng, B.F., Hesse, H., Kerrigan, E.C., Palacios, R. and Graham, J.M.R. (2014), "Efficient aeroservoelastic modeling and control using trailing-edge flaps of wind turbines", *Proceedings of the Control (CONTROL), 2014 UKACC International Conference on*. Loughborough, UK: IEEE.
- Øye, S. (1999), FLEX5 user manual. *Danske Techniske Høgskole*.
- Sun, X., Dai, Q., Menon, M. and Ponta, F. (2017), "Design and simulation of active external trailing edge flaps for wind turbine blades on load reduction", *J. Aerosp. Eng. - ASCE*, **30**(5).
- Tao, J., Sun, Y., Wu, G. and Yu, X. (2013), "Emulating the directional sensitivity of fish hair cell sensor", *J. Intel. Mat. Syst. Str.*, **24**, 1484-1493.
- Timmer, W. and Schaffarczyk, A. (2004), "The effect of roughness at high Reynolds numbers on the performance of aerofoil DU 97-W-300Mod", *Wind Energy*, **7**(4), 295-307.
- van Netten, S.M. (2006), "Hydrodynamic detection by cupulae in a lateral line canal: functional relations between physics and physiology", *Biological Cybernetics*, **94**(1), 67-85.
- van Wingerden, J.W., Hulskamp, A.W., Barlas, T., Marrant, B., van Kuik, G.A.M., Molenaar, D.P. and Verhaegen, M. (2008), "On the proof of concept of a 'Smart' wind turbine rotor blade for load alleviation", *Wind Energy*, **11**(3), 265-280.
- Viterna, L.A. and Janetzke, D.C. (1982), Theoretical and experimental power from large horizontal-axis wind turbines. National Aeronautics and Space Administration, Cleveland, OH (USA). Lewis Research Center.
- Wilson, D.G., Berg, D.E., Barone, M.F., Berg, J.C., Resor, B.R. and Lobitz, D.W. (2009), "Active aerodynamic blade control design for load reduction on large wind turbines", *Proceedings of the European Wind Energy Conference, Marseille, France*. 643-678.
- Wilson, D.G., Resor, B.R., Berg, D.E., Barlas, T.K. and Van Kuik, G.A. (2010), "Active aerodynamic blade distributed flap control design procedure for load reduction on the UpWind 5MW wind turbine", *Proceedings of the 48th AIAA Aerospace Sciences Meeting*. Orlando, FL, USA.
- Yu, X., Tao, J. and Berilla, J. (2010), "A bio-inspired flow sensor. *SPIE Smart Structures and Materials+ Nondestructive Evaluation and Health Monitoring*. International Society for Optics and Photonics, 764618-764618-764617.

CY